Draft version November 28, 2022
Typeset using LaTeX default style in AASTeX62

Expected Fragment Distribution from the First Interstellar Meteor CNEOS 2014-01-08

Amory Tillinghast-Raby,[1] Abraham Loeb,[1] and Amir Siraj[1]

[1]*Department of Astronomy, Harvard University, 60 Garden Street, Cambridge, MA 02138, USA*

ABSTRACT

The fireball of the first interstellar meteor, CNEOS 2014-01-08 (IM1) (Siraj & Loeb 2019), was detected off the northern coast of Papua New Guinea. A recently announced ocean expedition will retrieve any extant fragments by towing a magnetic sled across a 10 km x 10 km area of ocean floor approximately 300 km north of Manus Island (Siraj, Loeb, & Gallaudet 2022). We formulate a model that includes both the probabilistic mass distribution of meteor fragments immediately after the fragmentation event, the ablation of the fragments, and the geographic distribution of post-ablation fragments along the ground track trajectory of the bulk fragment cloud. We apply this model to IM1 to provide a heuristic estimate of the impactor's post-ablation fragment mass distribution, constructed through a Monte Carlo simulation. We find between $\sim 14\%$ and $\sim 36\%$ of IM1 fragments are expected to survive ablation with a mass $\geq .001$ g, and also provide an estimation for the geographic distribution of post-ablation fragments.

Keywords: Interstellar objects – Meteors – Bolides – Meteor fragmentation – Meteor ablation

1. INTRODUCTION

Two interstellar objects have been identified passing through the Solar System over the past five years: first Oumuamua' in 2017 (Meech et al. 2017), and then the comet Borisov in 2019 (Guzik et al. 2020). However, two interstellar meteors (IM) were detected before these reports. CNEOS 2014-01-08 (IM1) was detected in Earth's atmosphere by U.S Department of Defense (DoD) sensors at 2014-01-08 17:05:34 UTC. First identified as interstellar by Siraj & Loeb (2019), the Department of Defense later confirmed, "the velocity estimate reported to NASA is sufficiently accurate to estimate an interstellar trajectory," at the 99.999% confidence level (Shaw 2022). A second interstellar meteor candidate, CNEOS 2017-03-09 (IM2), was identified in September, 2022 (Siraj & Loeb 2022a). Based on the ram-pressure of the atmosphere at the point where the meteors disintegrated, Siraj & Loeb (2022a) concluded that both meteors had material strength tougher than iron indicating a source that is unlikely to be a planetary system like the Solar system.

The recovery of fragments from an interstellar object could provide direct material evidence for the chemical composition of its origin (Hawkes & Woodworth 1997). However, as meteor ablation is a strong function of entry velocity, a previous study concluded that any impactor with geocentric velocity > 28 km s^{-1} would likely ablate completely in Earth's atmosphere, and therefore any object traveling fast enough to be inferred as interstellar is unlikely to survive to Earth's surface (Hawkes & Woodworth 1997). We re-examine this conclusion on the basis that the previous work considers meteor ablation exclusively, but not fragmentation with which a change in net atmospheric velocity for the fragments is associated (Limonta et al. 2021).

The surface impact location relative to the point in the atmosphere where the meteor explodes is partially dependent on the post-ablation fragment mass because of deceleration due to dynamical drag. Constructing the post-ablation fragment mass distribution is consequently important for optimizing the search process. The outline of this paper is as follows. In Section 2 we present our mathematical formalism. In Section 3 we summarize the properties of IM1, and in Section 4 we apply our model to IM1. Our results are presented in Section 5, Section 6 and Section 7. Finally, we summarize our conclusions in Section 8.

amory_tillinghast-raby@alumni.brown.edu, aloeb@cfa.harvard.edu, amir.siraj@cfa.harvard.edu

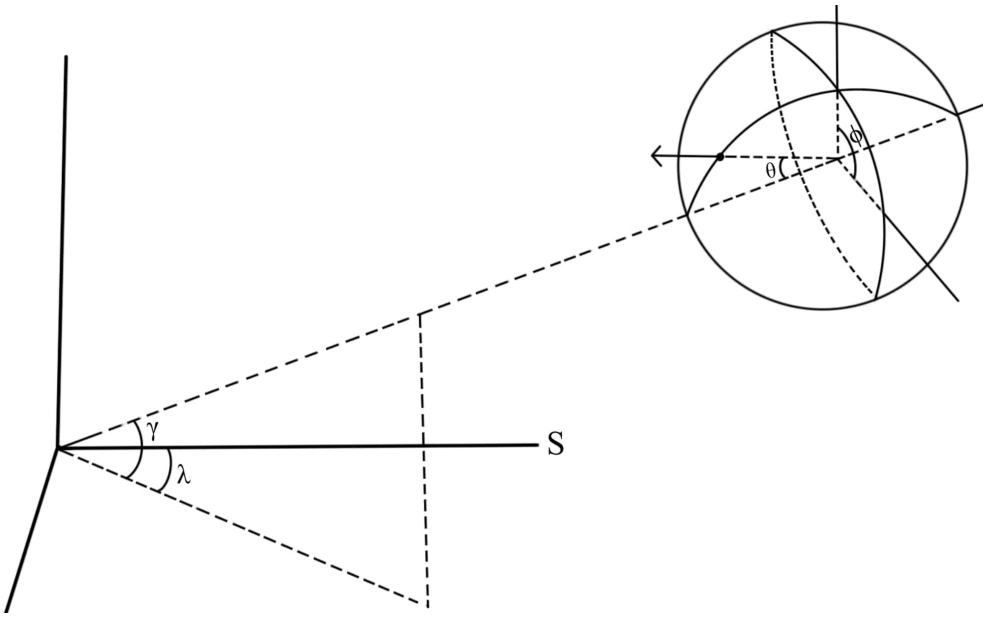

Figure 1. Spherical coordinate system around the meteor at the time of fragmentation. The impactor's trajectory is defined as its polar axis, (v, $\theta = 0$, $\phi = 0$). Angles $\theta \in [0, \pi]$ and $\phi \in [0, 2\pi]$ define the fragment ejection direction in the reference frame of the parent body. Angles $\gamma \in [0, \pi/2]$ and $\lambda \in [0, 2\pi]$ define the trajectory of the meteor and bulk fragment cloud relative to the ground.

2. MATHEMATICAL FORMULATION

2.1. *Fragmentation Model*

Because of the explosive nature of fragmentation, the distributions of both the pre-ablation fragment mass and the fragment ejection direction in the reference frame of the parent body must be taken into account. A version of the NASA Standard Breakup Model (SBM) derived for the atmospheric fragmentation of meteors (Limonta et al. 2021) provides the pre-ablation fragment mass distribution, defined as $p_{m_{initial}}$ in equation (1),

$$p_{m_{initial}} = \frac{f}{3\left(D_{\min}^{-f} - D_{\max}^{-f}\right)} \left(\frac{\pi}{6}\rho_m\right)^{f/3} m_{initial}^{-f/3-1}, \tag{1}$$

where f is an empirically determined fixed scale factor = 1.6, $D_{\min}$ is the diameter of the smallest fragment allowed by the distribution, and $D_{\max}$ is the diameter of the largest fragment allowed by the distribution. A power-law distribution accounts for the demonstrated fractal nature of high energy fragmentation events (Turcotte 1986) which holds strongly for meteoric entries (Limonta et al. 2021; Badyukov & Dudorov 2013; Fries et al. 2014).

There is no observational evidence of a preferred fragment ejection direction in the reference frame of the parent body (Limonta et al. 2021). Assuming a spherical geometry for the impactor, the ejection direction is taken to be uniform over the impactor's surface area (Frey & Colombo 2021) as shown in equation (2),

$$p_s = \frac{1}{4\pi r_i^2}, \tag{2}$$

where r_i is the impactor's radius. Note this is distinct from a uniform distribution over the spherical angles θ and ϕ (defined in Figure. 1), which subtly biases ejection towards the impactor's polar regions (Figure. 2). To find the angular distribution corresponding to a uniform ejection direction distribution over the surface, we follow Frey & Colombo (2021) and Weisstein (2002) and observe that for the coordinate system defined in Figure. 1, a differential unit of area on the impactor's surface is $ds = (r_i)^2 \sin(\theta) d\theta d\phi$. Therefore, the probability distribution function for a uniformly distributed ejection direction, expressed in terms of (θ, ϕ) is,

$$p_{\theta,\phi} = \frac{p_s ds}{d\theta d\phi} = \frac{\sin(\theta)}{4\pi}, \tag{3}$$

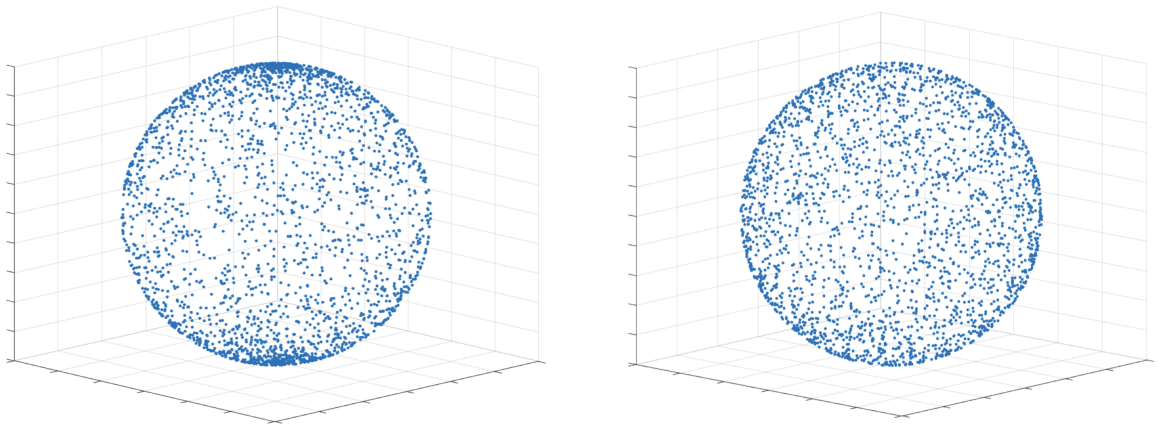

Figure 2. 2500 points randomly sampled from a sphere with $r_i = (1/2)D_{IM1}$. Left uniform distribution over (θ, ϕ). Right, uniform distribution over the surface in accordance with equation (3).

and the joint probability distribution for the pre-ablation fragment mass and angular ejection direction in the reference frame of the parent body, defined as $p_{m_{initial},\theta,\phi}$, is the product of equation (1) and equation (3),

$$p_{m_{initial},\theta,\phi} = \frac{f}{3\left(D_{\min}^{-f} - D_{\max}^{-f}\right)} \left(\frac{\pi}{6}\rho_m\right)^{f/3} m_{initial}^{-f/3-1} \frac{\sin(\theta)}{4\pi}. \tag{4}$$

2.2. *Ablation Model*

Classical meteor theory provides equations governing the deceleration and ablation of meteors (McKinley 1961; Passey & Melosh 1980; Bronshten 1983; Hawkes & Woodworth 1997; Trigo-Rodríguez et al. 2021),

$$\frac{\mathrm{d}v}{\mathrm{d}t} = -\frac{\Gamma\rho_{\mathrm{a}}v^2}{m} A \left(\frac{m}{\rho_{\mathrm{m}}}\right)^{2/3}, \tag{5}$$

$$\frac{\mathrm{d}m}{\mathrm{d}t} = -\frac{\Lambda}{2\zeta} A \left(\frac{m}{\rho_m}\right)^{2/3} \rho_a v^3, \tag{6}$$

where v is the instantaneous atmospheric fragment speed, m is the instantaneous fragment mass, Γ is a dimensionless drag coefficient, Λ is a dimensionless heat transfer coefficient, ζ is the heat of ablation (defined as the summed heats of fusion and vaporization), ρ_m is the material density of the impactor, and ρ_a is the atmospheric density. "A" is a shape factor defined such that $A\,(m/\rho_m)^{2/3}$ equals the cross sectional area of the impactor. Assuming a spherical geometry, the value of "A" follows directly from solving for the cross-sectional area in terms of impactor volume. We define Ω to be the impactor's cross sectional area. Then, $\Omega = \pi\,(3/4\pi)^{(2/3)}\,(m/\rho_m)^{(2/3)} = 1.21\,(m/\rho_m)^{(2/3)}$. For a sphere, $A = 1.21$. The trajectory of the bulk fragment cloud is given by,

$$\frac{dz}{dt} = -v\sin(\gamma), \tag{7}$$

$$\frac{dx}{dt} = v\sin(\lambda)\cos(\gamma), \tag{8}$$

$$\frac{dy}{dt} = v\cos(\lambda)\cos(\gamma), \tag{9}$$

where z is the altitude, γ is the angular trajectory relative to the ground, λ is the azimuth, x is the position along the East-West axis relative to the airburst location, and y is the position along the North-South axis relative to the airburst location. Lastly, the atmospheric density profile is given by, $\rho_a = \rho_0 e^{(-z/H)}$, where ρ_0 is the sea-level atmospheric density, and $H = 8$ km is the scale height of the atmosphere (Collins et al. 2005).

3. IM1

The meteor IM1 was detected traveling at $v_{IM1} = 44.8$ km s^{-1} with $\gamma = .468$ and $\lambda = 4.98$ (Zuluaga 2019). The total mass of the impactor was calculated as approximately M $\sim 5 \times 10^5$ g (Siraj & Loeb 2019). Three distinct flares are apparent in the meteor's light curve between altitudes 23 km and 18.7 km, with the largest flare occurring at 18.7 km which is taken to be the "gross" fragmentation altitude (Ceplecha et al. 1993). Further analysis of the light curve provides the total explosion energy, $E = 5 \times 10^{18}$ erg, and the yield strength of the meteor, Y_{IM1} ~113 MPa (Siraj & Loeb 2022b), which is more than twice the yield strength of iron meteorites.

4. MODEL APPLICATION TO IM1

The strongest known class of meteorites is iron (Petrovic 2001). Therefore, to provide a heuristic baseline estimate of the post-ablation fragment mass distribution of IM1, we adopt the corresponding material properties of iron.

4.1. *Fragmentation of IM1*

The density of iron is $\rho_{\rm m} = 8$ g cm^{-3}. The implied diameter of the meteor, assuming a spherical geometry, is $D_{IM1} = 50$ cm. We choose $D_{\rm min} = 0.1$ cm, the smallest fragment diameter allowed by the empirical bounds of the NASA SBM (Krisko 2011), and $D_{\rm max} = 0.7 D_{IM1}$, as the upper limit of the distribution (Limonta et al. 2021). From equation (4), the joint pre-ablation fragment mass, angular ejection direction distribution function for IM1 is then,

$$p_{m_{initial},\theta,\phi} = \frac{f}{3\left(0.1^{-f} - 0.7 D_{IM1}^{-f}\right)} \left(\frac{8\pi}{6}\right)^{f/3} m_{initial}^{-f/3-1} \frac{\sin(\theta)}{4\pi} \tag{10}$$

Given the explosion energy, E, we calculate the instantaneous fragment ejection speed in the reference frame of the parent body to be ≈ 41 km s^{-1}.

$$v_{\rm ejection} = \sqrt{\frac{2\beta E}{M}} \approx 41 \text{ km s}^{-1} \tag{11}$$

$\beta = .93$ is a fractional coefficient accounting for the portion of explosion energy known to be lost to radiation (Siraj & Loeb 2022b). To calculate the initial atmospheric speed of an ejected fragment, defined as v_0, we take the norm of the sum of the IM1 trajectory vector ($v_{IM1} = 44.8$ km s^{-1} , $\theta = 0$, $\phi = 0$) and ejection vector ($v_{ejection} = 41$ km s^{-1}, θ, ϕ) for a given (θ, ϕ). As shown in Figure. 3, for a given value of θ, v_0 is constant across all ϕ.

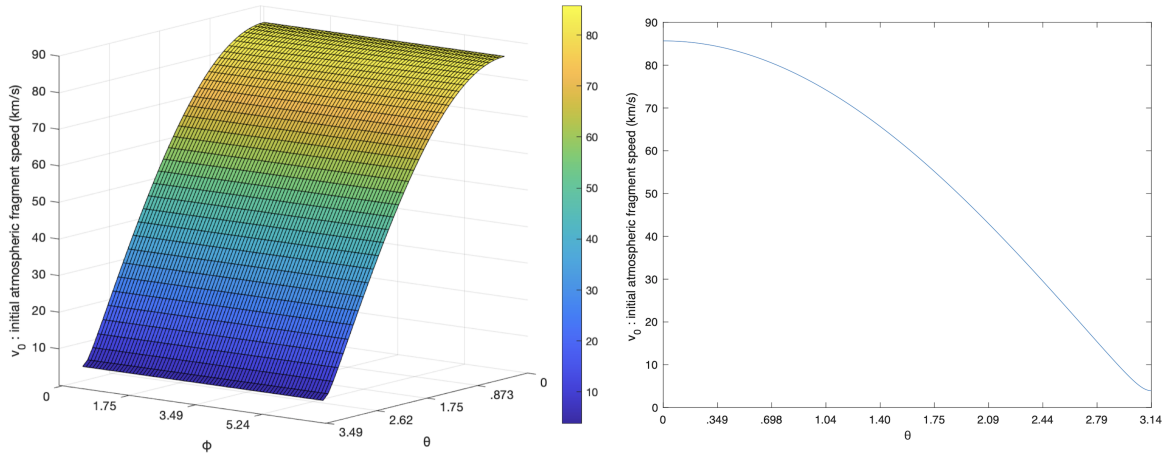

Figure 3. Left, initial atmospheric fragment speed, v_0 as a function of θ, ϕ. Right, two dimensional cross section of the initial atmospheric fragment speed surface.

4.2. *Ablation and Trajectory of IM1 Fragments*

The heat of ablation of iron is $\zeta = 6.549 \times 10^{10}$ erg g^{-1}. Previous studies on the ablation of iron meteors adopt a constant value for the dimensionless heat transfer coefficient, $\Lambda = .02$ (Passey & Melosh 1980). Since the ablation rate

is highly dependent on Λ, we conservatively use double this value, $\Lambda = .04$. For spherical bodies, the dimensionless drag coefficient is, $\Gamma = .5$ (Passey & Melosh 1980; Hawkes & Woodworth 1997).

To calculate the ablation and surface impact location for a given pre-ablation fragment mass, $m_{initial}$, and ejection angle in the reference frame of the parent body, (θ, ϕ), we first calculate the initial atmospheric fragment speed, v_0, by taking the norm of the sum of the IM1 trajectory vector and the fragment ejection vector in accordance with section 4.1. We then integrate equations (5) through (9) starting at $m_{initial}$, v_0, the gross fragmentation altitude $z_0 = 18.7$ km, and the fragmentation site ($x = 0$ km, $y = 0$ km), along the angular trajectory of the bulk fragment cloud relative to the ground ($\gamma = .468$, $\lambda = 4.98$). The integration is computed with a variable step, variable order (VSVO) integrator optimized for stiff differential systems. At each step we check that the fragment has not decelerated past its terminal velocity, and reset the velocity to its terminal value if this condition is not met.

The ablative process is rapid. For $m_{initial} \in [.0041\text{ g}, 3\text{ g}]$ and $\theta \in [0, 2.93]$ (86 km s^{-1} $\geq v_0 \geq$ 10 km s^{-1}), which accounts for 96% of the joint distribution described in equation (10) after integrating over all ϕ as shown in equation (12), ablation concludes at approximately z_0 (Figure. 4).

$$\int_{.0041}^{3.0}\int_{0}^{2.93}\int_{0}^{2\pi}\left(\frac{f}{3\left(0.1^{-f}-.7D_{IM1}^{-f}\right)}\left(\frac{8\pi}{6}\right)^{f/3}m_{initial}^{-f/3-1}\frac{\sin(\theta)}{4\pi}\right)d\phi d\theta dm_{initial} = .96 \tag{12}$$

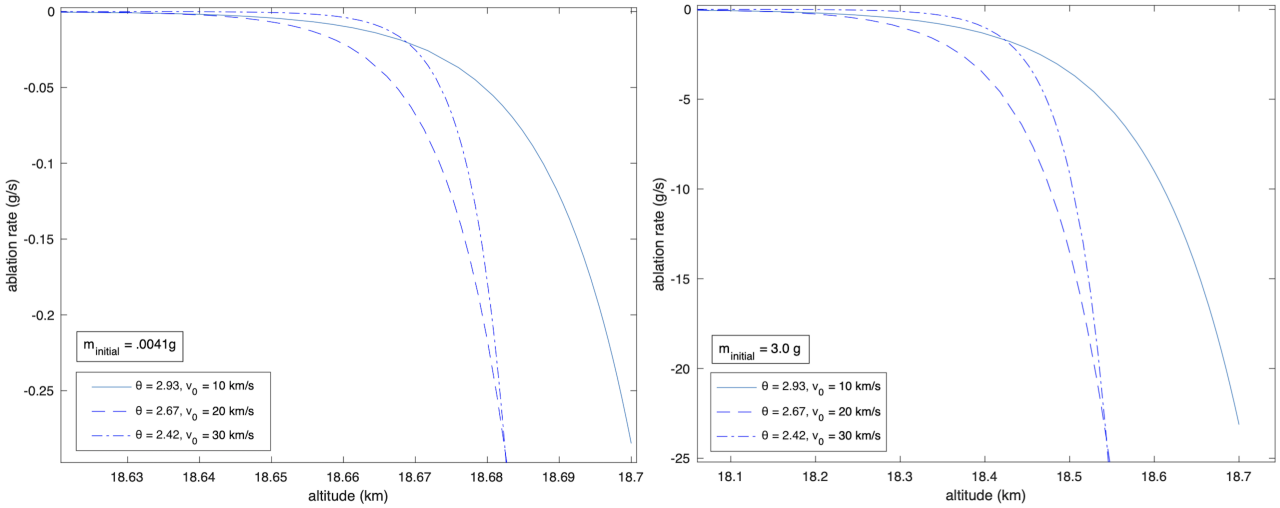

Figure 4. Altitude vs ablation for $m_{initial} = .0041$ g, $m_{initial} = 3.0$ g and $v_0 = 10$ km s^{-1}, $v_0 = 20$ km s^{-1}, and $v_0 = 30$ km s^{-1}. $z_0 = 18.7$ km, the gross fragmentation altitude. The ablation rate is expressed as negative following from the definition of equation (6).

5. DERIVED PROBABILITY DISTRIBUTION OF THE POST-ABLATION FRAGMENT MASS

We define the probability distribution of the post-ablation fragment mass to be $p_{m_{final}}$. The distribution was constructed numerically via a Monte Carlo Simulation. 5×10^6 $(m_{initial}, \theta, \phi)$ vectors were randomly sampled from equation (10). The post-ablation mass, defined as m_{final}, and surface impact site corresponding to each $(m_{initial}, \theta, \phi)$ vector was calculated in accordance with section 4.2. The probability distribution function of the post-ablation fragment masses, defined as $p_{m_{final}}$ was then computed as a normalized histogram (Figure. 5).

As expected from empirical studies on recovered meteor fragments (Badyukov & Dudorov 2013; Fries et al. 2014), the distribution $p_{m_{final}}$ has the structure of a power law. Summing the area under the normalized histogram for $m_{final} \geq .001$ g, we find that 14.43% of IM1 fragments survive ablation with a mass $m_{final} \geq .001$ g.

From section 3, the total mass of IM1 was calculated to be, M $\sim 5 \times 10^5$ g (Siraj & Loeb 2019). Following Limonta et al. (2021), the total number of fragments produced during the airburst is calculated as,

$$N = \frac{M}{\int_{m_{\min}}^{m_{\max}} m p_m dm} = 2.90 \times 10^4 \tag{13}$$

where $m_{min} = \rho_m(4/3)\pi(D_{min}/2)^3 = 4.10 \times 10^{-3}$ g and $m_{max} = \rho_m(4/3)\pi(D_{max}/2)^3 = 1.79 \times 10^5$ g. The expected number of fragments in five subdivisions of the post-ablation mass range $m_{final} \geq .001$ g as well as the specific probability of each subdivision is plotted in Figure. 6.

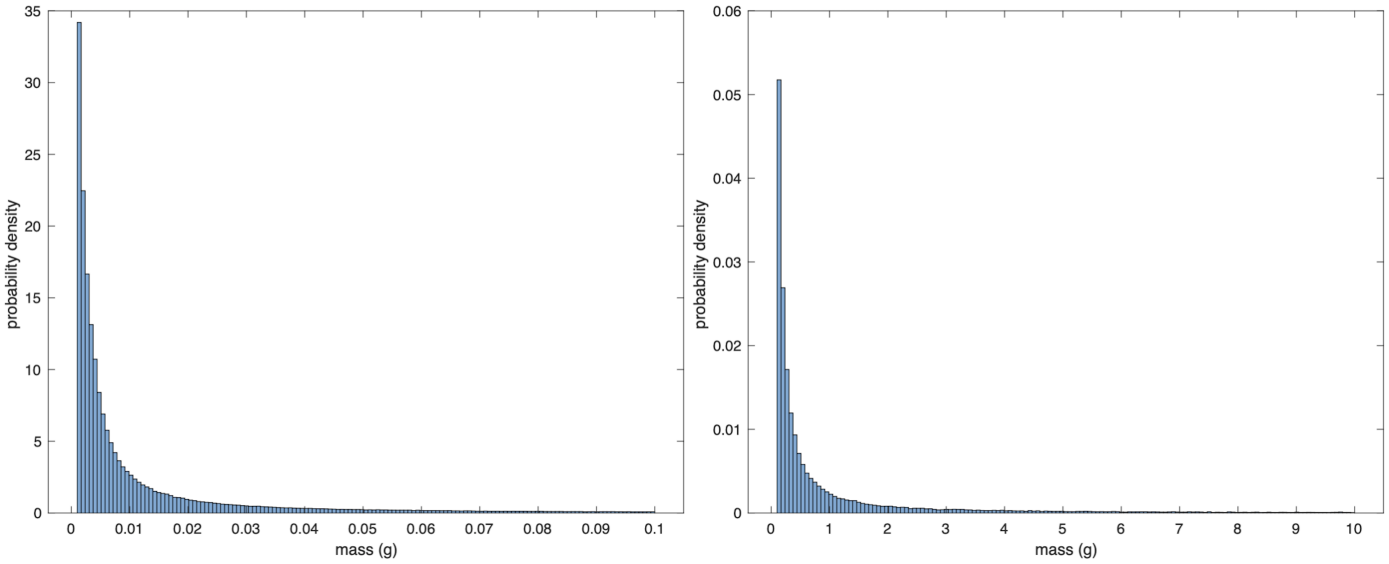

Figure 5. Post-ablation fragment mass probability density histogram over the regions, $m_{final} \in [.001 \text{ g}, .1 \text{ g}]$ and $m_{final} \in [.1 \text{ g}, 10 \text{ g}]$

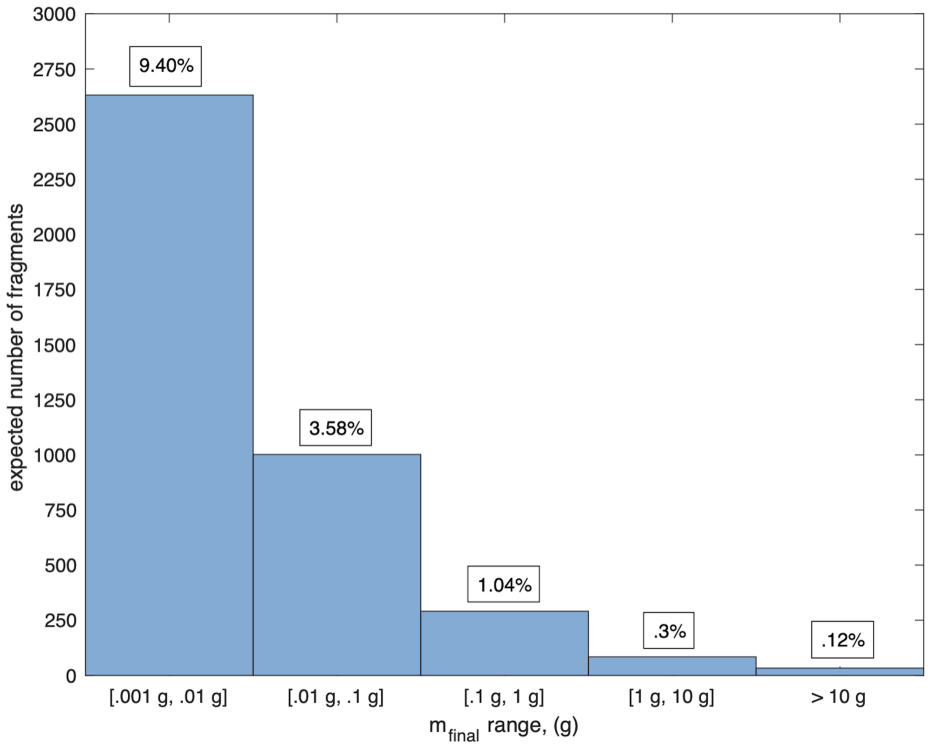

Figure 6. Percentage of fragments surviving with a post-ablation mass in the given ranges and the expected number of fragments in each range.

6. GEOGRAPHIC DISTRIBUTION

The trajectory of IM1's bulk fragment cloud followed a northwestern track over the ground ($\lambda = 4.98$). In Figure. 7, we define the location of the IM1 airburst as the origin ($x = 0$ km, $y = 0$ km). We then plot the approximate surface impact site along the line drawn by the trajectory of IM1's bulk fragment cloud for post-ablation masses $m_{final} \in [.001\text{ g}, 10\text{ g}]$. This mass range accounts for 14.31% of all post-ablation fragments and 99.2% of post-ablation fragments with a mass $\geq .001$ g. We include the normalized marginal histograms for the western and northern impact coordinates of the fragments.

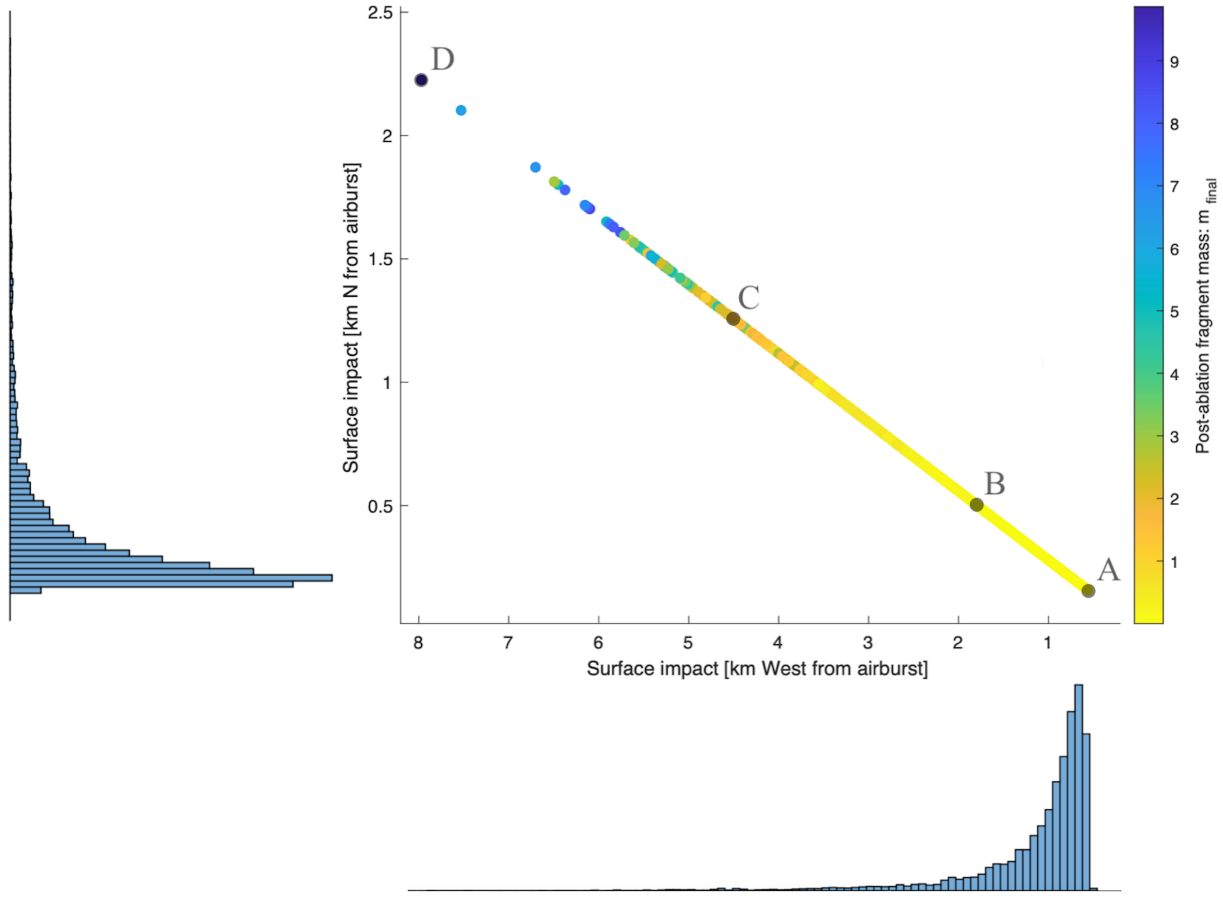

Figure 7. Surface impact location and marginal histograms for the western and northern impact coordinates of 10×10^3 post-ablation fragment masses, $m_{final} \in [.001\text{ g}, 10\text{ g}]$. The impact site is a strong function of mass, with larger post-ablation masses landing further from the fragmentation site.

To estimate the concentration of fragments, we sum the area under the northern impact coordinate histogram in subdivisions of the range $y \in [.15\text{ km}, 2.2\text{ km}]$ and the western impact coordinate histogram in subdivisions of the range $x \in [.55\text{ km}, 8.0\text{ km}]$. 87% of considered post-ablation fragments (~ 3600 fragments) are expected to fall approximately along the 1.34 km length between points "A" ($x = .55$ km, $y = .15$ km) and "B" ($x = 1.85$ km, $y = .50$ km) drawn out by the bulk trajectory of the IM1 fragment cloud. This region predominately contains fragments with a post-ablation mass $m_{final} \in [.001\text{ g}, .1\text{ g}]$.

11.2% of considered post-ablation fragments with a mass $\geq .001$ g (~ 470 fragments) are expected to fall approximately along the 2.75 km length between points "B" and "C" ($x = 4.50$ km, $y = 1.25$ km). This region predominately contains fragments with a post-ablation mass $m_{final} \in [.1\text{ g}, 2\text{ g}]$.

The remaining $\sim 1.8\%$ of considered post-ablation fragments with a mass $\geq .001$ g (~ 75 fragments) are estimated to fall approximately along the 3.62 km length between points "C" and "D" ($x = 7.97$ km, $y = 2.23$ km). This final region predominately contains fragments with a post-ablation mass, $m_{final} \in [2\text{ g}, 10\text{ g}]$.

7. ADDITIONAL CONSTRAINTS ON THE 1M1 FRAGMENT MASS DISTRIBUTION

As iron is the strongest known class of meteorites (Petrovic 2001), the previous sections assumed an iron material for IM1 which has a yield strength, $Y_{iron} = 50$ MPa. However, the calculated yield strength of IM1 is $Y_{IM1} \sim 113$ MPa. Therefore, to bracket the post-ablation fragment mass distribution in terms of the strength of the impactor, we now consider the post-ablation fragment mass distribution assuming a generic steel material, $Y_{steel} = 250$ MPa.

7.1. *Fragmentation of IM1 Assuming a Steel Material*

The density of steel is $\rho_{\mathrm{m_{steel}}} = 8$ g cm^{-3} and the implied diameter of IM1 is $D_{IM1_{steel}} = 50$ cm. With reference to equation (1), for the maximum fragment diameter produced during the airburst we again adopt $D_{\mathrm{max}_{steel}} = .7D_{IM1_{steel}}$. We scale the minimum fragment diameter, $D_{\mathrm{min}_{steel}}$, in proportion to the increase in yield strength of steel versus iron. Therefore, $D_{\mathrm{min}_{steel}} = .5$ cm. The pre-ablation fragment mass distribution assuming a generic steel material is,

$$p_{m_{initial,steel}} = \frac{f}{3\left(.5^{-f} - .7D_{IM1_{steel}}^{-f}\right)}\left(\frac{8\pi}{6}\right)^{f/3} m_{initial,steel}^{-f/3-1}, \tag{14}$$

and the joint distribution for the pre-ablation fragment mass and angular ejection direction in the reference frame of the parent body is,

$$p_{m_{initial,steel},\theta,\phi} = \frac{f}{3\left(.5^{-f} - .7D_{IM1_{steel}}^{-f}\right)}\left(\frac{8\pi}{6}\right)^{f/3} m_{initial,steel}^{-f/3-1}\frac{\sin(\theta)}{4\pi}. \tag{15}$$

7.2. *Ablation of IM1 Fragments Assuming a Steel Material*

The thermal properties of steel are comparable to thermal properties of iron. The heat of ablation of steel is $\zeta_{steel} = 6.747 \times 10^{10}$ erg g^{-1} (Chawla et al. 1981) and we again choose the dimensionless heat transfer coefficient as $\Lambda_{steel} = .04$. We randomly sample 5×10^6 $(m_{initial,steel}, \theta, \phi)$ vectors from equation (15) and calculate each fragment's post-ablation mass, defined as $m_{final,steel}$, in accordance with Section 4.2. We then construct the derived post-ablation fragment mass distribution assuming a steel material, defined as $p_{m_{final,steel}}$, as a normalized histogram depicted in Figure. 8.

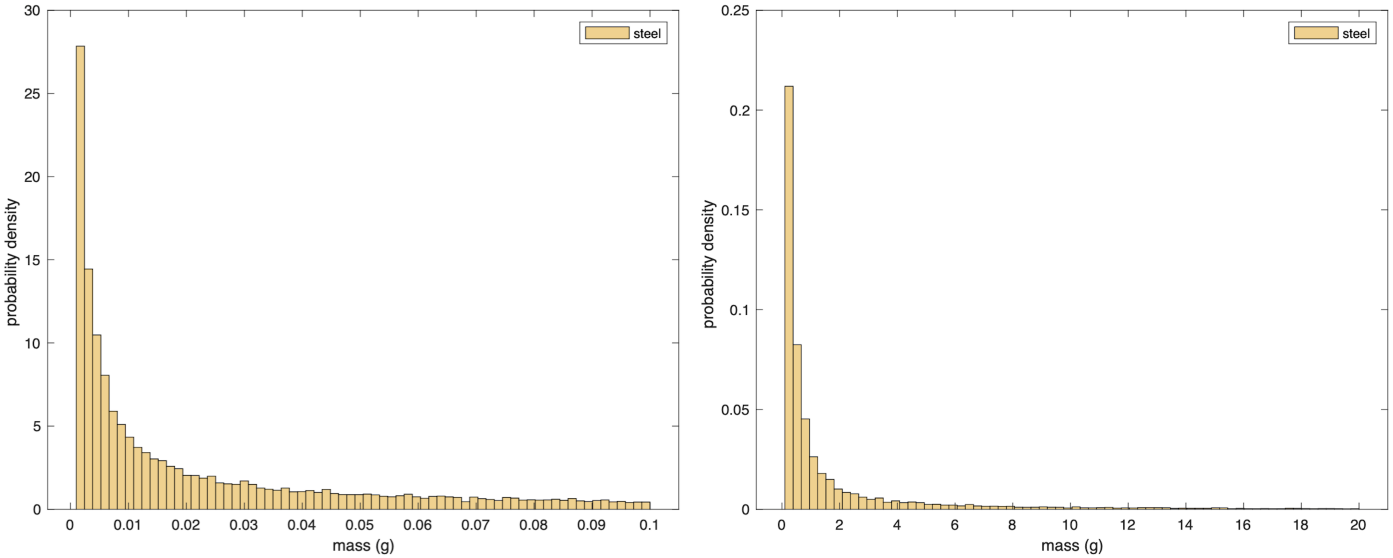

Figure 8. Post-ablation fragment mass probability density histogram over the regions, $m_{final,steel} \in [.001\text{ g}, .1\text{ g}]$ and $m_{final,steel} \in [.1\text{ g}, 20\text{ g}]$

By summing the area under the normalized histogram for $m_{final,steel} \geq .001$ g we find that assuming a steel material, $\sim 36.08\%$ of fragments survive with a mass $m_{final,steel} \geq .001$ g. This is in comparison to the $\sim 14.43\%$ of fragments that are expected survive with a mass $m_{final} \geq .001$ g when assuming an iron material.

The total number of fragments produced during the airburst is calculated as,

$$N = \frac{M}{\int_{m_{\min,steel}}^{m_{\max,steel}} m p_{m_{initial,steel}} dm} = 2.24 \times 10^3, \tag{16}$$

where $m_{min,steel} = \rho_m(4/3)\pi(D_{min,steel}/2)^3 = 5.10 \times 10^{-1}$ g and $m_{max,steel} = \rho_m(4/3)\pi(D_{max,steel}/2)^3 = 1.79 \times 10^5$ g. From equation (16), we see that because of steel's higher yield strength in comparison to iron, fewer fragments are expected to be produced during the airburst. However, the fragments produced have a greater mass from a smaller possible range $[5.10 \times 10^{-1}$ g, 1.79×10^5 g].

We calculate the expected number of fragments in five subdivisions of the post-ablation mass range $m_{final,steel} \geq .001$ g as well as the specific probability of each subdivision and plot the results in Figure. 9 below.

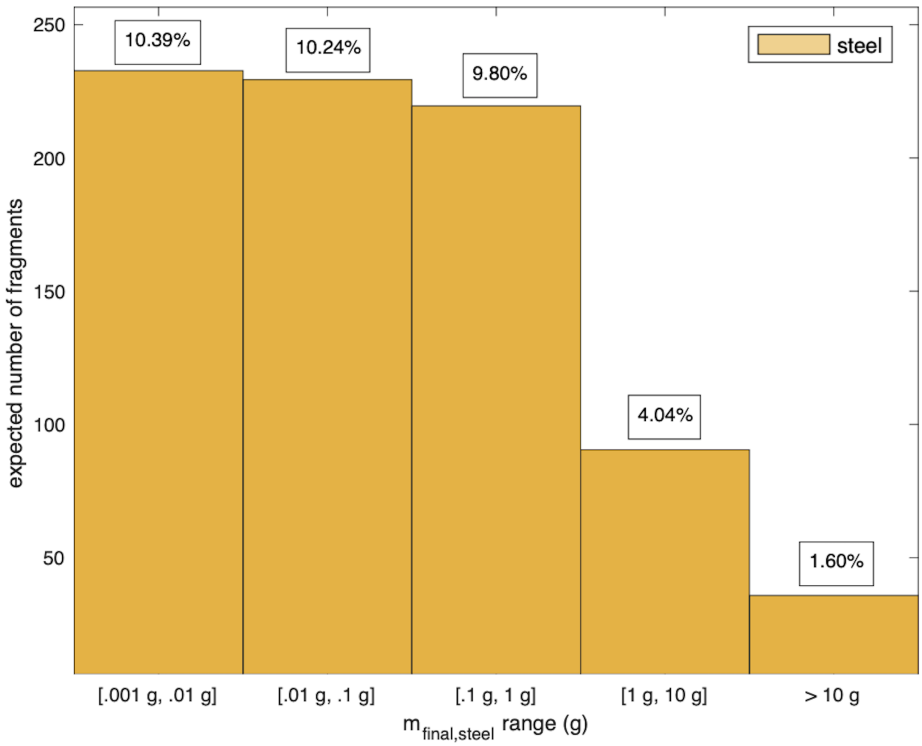

Figure 9. Percentage of fragments surviving with a post-ablation mass in the given ranges and the expected number of fragments in each range.

As shown in Figure. 9, while the percentages of fragments with a post-ablation mass in each subdivison are higher than the corresponding percentages assuming an iron material, the numbers of fragments in the ranges $m_{final,steel} \in [.001$ g, $.01$ g$]$, $m_{final,steel} \in [.01$ g, $.1$ g$]$, and $m_{final,steel} \in [.1$ g, 1 g$]$ are fewer than the corresponding number of fragments assuming an iron material. For larger post-ablation fragment masses, $m_{final,steel} \in [1$ g, 10 g$]$ and $m_{final,steel} > 10$ g, we expect on the order of tens of fragments.

8. CONCLUSION

An earlier study concluded meteors with a geocentric velocity > 28 km s^{-1} would likely ablate completely in Earth's atmosphere and therefore any object traveling fast enough to be inferred as interstellar would be unlikely to survive to the Earth's surface (Hawkes & Woodworth 1997). By considering how the atmospheric velocity change due to fragmentation affects ablation, we have found that even for a parent body speed as high as 44.8 km s^{-1}, a significant portion of meteor fragments could survive ablation. In the case of IM1, we estimate assuming an iron material that 14.43% of IM1 fragments survive ablation with a final mass $\geq .001$ g.

Of these 14.43% of fragments, 89.95% have a mass $\in [.001$ g, $.1$ g$]$. The majority of this fragment group is expected to fall approximately along a 1.34 km length immediately to the northwest of the airburst (Figure. 7, Segment "A-

B"). The optimal search area for small fragment recovery is therefore approximately under the airburst site. Larger fragments are expected to be distributed approximately along the line drawn by the bulk trajectory of the IM1 fragment cloud, at a distance greater than $\sim$ .50 km north and $\sim$ 1.85 km west (Figure. 7, Segment "B-C" and Figure. 7, Segment "C-D").

To bracket the post-ablation fragment mass distribution based on material strength, we calculate the post-ablation fragment mass distribution based on a steel material. Assuming the properties of steel, we estimate 36.08% of fragments survive ablation with a post-ablation mass $\geq$ .001 g with tens of fragments surviving with a post-ablation mass $\geq$ 10 g. The empirical post-ablation fragment mass distribution of IM1 should fall between the two estimations calculated in the preceding sections.

ACKNOWLEDGEMENTS

This work was supported in part by the Galileo Project at Harvard University.

REFERENCES

Badyukov, D. D., & Dudorov, A. E. 2013, Geochemistry International, 57, 583.

Bronshten, V. A. 1983, Physics of Meteoric Phenomena, (Nauka,Moscow,1981;Reidel,Dordrecht,1983).

Chawla, T.C., Graff, D.L., Borg, R.C., et al. 1981, Nuclear Engineering and Design, 67, 57

Ceplecha, Z., Spurny, P., Borovicka, J., et al. 1993, A&A, 279, 615.

Collins, G. S., Melosh, H. J., & Marcus, R. A. 2005, M&PS, 40, 817

Frey, S., & Colombo, C. 2021, Journal of Guidance, Control, and Dynamics, 44, 88

Fries, M., Le Corre, L., Hankey, M., et al. 2014, M&PS, 49, 1989

Guzik, P., Drahus, M., Rusek, K., et al. 2020, Nature Astronomy, 4, 53

Hawkes, R. L., & Woodworth, S. C. 1997, Journal of the Royal Astronomical Society of Canada, 91

Krisko, P. H. 2011, Orbital Debris Quarterly News, 15, 1

Limonta, S., Trisolini, M., Frey, S., et al. 2021, Icarus, 367

McKinley, D. W. R. 1961, Meteor Science and Engineering, New York

Meech, K. J., Weryk, R., Micheli, M., et al. 2017, Nature, 552, 378

Passey, Q. R., & Melosh, H. J. 1980, Icarus, 42, 211

Petrovic, J. J. 2001, Journal of Materials Science, 36, 1579

Register, P. J., Mathias, D. L., & Wheeler, L. F. 2017, Icarus, 284, 157

Shaw, J. E. 2022, Department of Defense, Confirmation of Interstellar Object, https://twitter.com/USSpaceCom/status/1511856370756177921?s=20&t=vzmmhRf6WthBaCt7BGzReA

Siraj, A., & Loeb, A. 2019, ApJ in press, arXiv:1904.07224

Siraj, A., Loeb, A., & Gallaudet, T. 2022, arXiv preprint, arXiv:2208.00092

Siraj, A., & Loeb, A. 2022a, arXiv preprint, arXiv:2209.09905

Siraj, A., & Loeb, A. 2022b, Res.Notes AAS, 6, 81

Tabetah, M. E., & Melosh, H. J. 2018, M&PS 53, 493

Turcotte, D. L. 1986, Journal of Geophysical Research, 91(B2), 1921

Trigo-Rodríguez, J. M., Dergham, J., Gritsevich, M., et al. 2021, Advances in Astronomy, 2021

Weisstein, E. W. 2002, Sphere Point Picking, From Mathworld - A Wolfram Web Resource, https://mathworld.wolfram.com/SpherePointPicking.html

Zuluaga, J. I. 2019, Res.Notes AAS, 3, 68